

# SCIENTIFIC REPORTS



OPEN

## Investigation on the structures and magnetic properties of carbon or nitrogen doped cobalt ferrite nanoparticles

Derang Cao<sup>1,2</sup>, Lining Pan<sup>2</sup>, Jianan Li<sup>2</sup>, Xiaohong Cheng<sup>2</sup>, Zhong Zhao<sup>1</sup>, Jie Xu<sup>1</sup>, Qiang Li<sup>1</sup>, Xia Wang<sup>1</sup>, Shandong Li<sup>1</sup>, Jianbo Wang<sup>2</sup> & Qingfang Liu<sup>2</sup>

Carbon or nitrogen doped cobalt ferrite nanoparticles were synthesized in the air by a facile calcination process. X-ray diffraction, mapping, X-ray photoelectron spectroscopy, and mössbauer spectra results indicate that the nonmetal elements as the interstitial one are doped into cobalt ferrite nanoparticles. The morphologies of doped cobalt ferrite nanoparticles change from near-spherical to irregular cubelike shapes gradually with the increased carbon or nitrogen concentration, and their particles sizes also increase more than 200 nm. Furthermore, the saturation magnetization of carbon doped cobalt ferrite is improved. Although the saturation magnetization of N-doped cobalt ferrite is not enhanced obviously due to the involved hematite, they also do not drop drastically. The results reveal an approach to synthesize large scale ferrite nanoparticles, and improve the magnetic properties of ferrite nanoparticles, and also provide the potential candidates to synthesis co-doped functional magnetic materials.

As is well-known, doping is a vitally common and important approach to modify the structures and properties of the materials by changing the ions distribution during the synthesis process<sup>1–8</sup>. The doping materials present the satisfying properties for lots of advanced applications such as battery<sup>9</sup>, capacitance<sup>10</sup>, electronic device<sup>11</sup>, catalysis<sup>12</sup>, etc. Lots of these properties and applications recently show a close relation with magnetic nanoparticles<sup>3,6,13–15</sup>, which requires the good magnetism of materials. Large magnetization, suitable particle size, and good dispersibility of the magnetic nanoparticles are desirable for the magnetic labels of biodetection<sup>16</sup>. However, the magnetization of the particles with smaller size (usually less than 20 nm) is less than that of the microbeads and the submicro or nanoparticles<sup>17</sup>. This work demonstrated a facile approach to synthesize large scale ferrite nanoparticles, and improved the magnetic properties of nanoparticles.

Generally, both metal and nonmetal elements are the normal origin of doping elements. The metal elements are more inclined to be doped into many magnetic materials<sup>3,4,6,18–23</sup> and some nonmagnetic materials<sup>10,12,24,25</sup>, while the nonmetal elements (like carbon, nitrogen, phosphor, and sulfur, etc.) usually focus on the doping of nonmagnetic materials, such as titanium dioxide<sup>26,27</sup>, carbon materials<sup>28,29</sup>, silicon materials<sup>30,31</sup> and other nonmagnetic materials<sup>11,24,32</sup>. This is due to the doped nonmetal elements can influence the electronic mobility or the band gap of crystal<sup>30,33,34</sup>, and thus improves the properties of these nonmagnetic materials. However, it is more inclined to be doped with the metal elements for the magnetic materials<sup>35–43</sup>, and these results only present in the theory researches<sup>44,45</sup> and a small number in experimental magnetic films<sup>46–50</sup>, which are prepared by vacuum deposition<sup>46–50</sup> or chemical vapor deposition<sup>51,52</sup>. The reason is that it is difficult for the nonmetal elements to be doped into the lattice of magnetic films<sup>53</sup>, and they always lies in the gap or the edge of the atom as a interstitial one, which is easy to achieve doping under vacuum condition<sup>46–50</sup>. Whereas, the metal elements can change the site preference of magnetic materials, and locate the lattice of magnetic materials, and further influence the magnetic properties of the samples<sup>35,54,55</sup>. As a result, the reports on the doping of nonmetal elements into magnetic nanoparticles are infrequent, and it should be considered.

<sup>1</sup>College of Physics, Laboratory of Fiber Materials and Modern Textile, the Growing Base for State Key Laboratory, Qingdao University, Qingdao, 266071, China. <sup>2</sup>Key Laboratory for Magnetism and Magnetic Materials of the Ministry of Education, Lanzhou University, Lanzhou, 730000, China. Correspondence and requests for materials should be addressed to D.C. (email: caoderang@163.com)

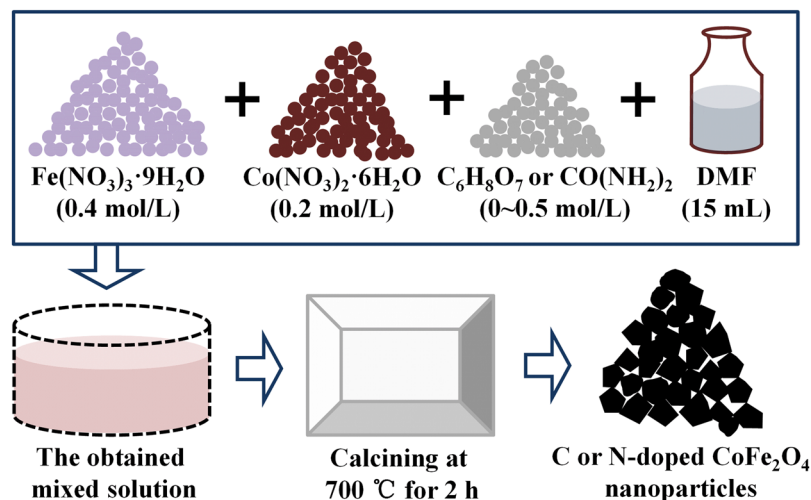


**Figure 1.** Schematic diagram of the simple experimental process.

Cobalt ferrite ( $\text{CoFe}_2\text{O}_4$ ), as a particularly important magnetic material, owns large magneto-crystalline anisotropy, high coercivity, large magnetostriction coefficient, and high saturation magnetization ( $M_s$ ), and it has attracted the considerable attention for a long time<sup>56–59</sup>. Numerous investigations on the doping of  $\text{CoFe}_2\text{O}_4$  nanoparticles have been reported including their structures and magnetic properties<sup>3–5,19,21,39,40,42,60–65</sup>. As mentioned above, nevertheless, the main studies of  $\text{CoFe}_2\text{O}_4$  nanoparticles also focused on the doping of metal elements (i.e. Li<sup>19</sup>, Mn<sup>21</sup>, Zn<sup>66</sup>, Ni<sup>67</sup>, Ga<sup>62</sup>, Dy<sup>60</sup>, In<sup>40</sup>, Bi<sup>4</sup>, Gd<sup>68</sup>, Cr<sup>69</sup>, Er<sup>39</sup>, Ho<sup>63</sup>, Ti<sup>70</sup>, La<sup>56</sup>, Ce<sup>36</sup>, RE<sup>35,71,72</sup>, etc.). These metal elements always substitute Fe or Co ions, and locate the lattice of  $\text{CoFe}_2\text{O}_4$  nanoparticles. The  $M_s$  of  $\text{CoFe}_2\text{O}_4$  nanoparticles often decreases after the doping due to the smaller magnetic moments of doped metal elements than that of the Fe or Co ions, and it is unsuitable for high  $M_s$  applications. There are only a few works showing the improvement of  $M_s$  after doping with metal elements<sup>4,21,69</sup>. The changed  $M_s$  are mainly affected by the site preference of tetrahedral (A) and octahedral (B) of Fe or Co ions. Saturation magnetization  $M_s$  is equal to the difference of the magnetizations of the two sites, i.e.,  $M_s = (\mu_B - \mu_A)$ , where  $\mu_B$  and  $\mu_A$  are the magnetizations of B and A sites respectively<sup>21</sup>. Until now, reports regarding the structures and magnetic properties of nonmetal doped  $\text{CoFe}_2\text{O}_4$  nanoparticles are less. Our recent work<sup>5</sup> studied the results of sulfur doped  $\text{CoFe}_2\text{O}_4$  nanoparticles, and the results showed an enhanced  $M_s$  after the doping. However, carbon or nitrogen doped  $\text{CoFe}_2\text{O}_4$  nanoparticles have not been demonstrated, and their results are still unclear.

In this work, series of nonmetal carbon or nitrogen doped  $\text{CoFe}_2\text{O}_4$  particles were prepared in the air via a facile calcination process, and this approach is different from the previous vacuum deposition method<sup>46–50</sup> and chemical vapor deposition<sup>51,52</sup> technique in the doping of nonmetal elements. There are no pH regulation, gas atmosphere, centrifugation and any another supplementary reagents during the preparing process. Various characterizations showed that carbon or nitrogen contents were doped into  $\text{CoFe}_2\text{O}_4$  nanoparticles, and the  $M_s$  of doped  $\text{CoFe}_2\text{O}_4$  nanoparticles was improved with the increased doping concentration. Combining our previous S-doped  $\text{CoFe}_2\text{O}_4$  nanoparticles<sup>5</sup>, the results reveal an approach to improve the magnetic properties of ferrite nanoparticles.

## Experimental

Ferric nitrate (0.4 mol·L<sup>-1</sup>), cobalt nitrate (0.2 mol·L<sup>-1</sup>) and various concentrations of citric acid (or urea) were dissolved in Dimethyl Formamide (DMF, 15 mL). The synthesis process can be simply described as  $\text{Fe}(\text{NO}_3)_3 + \text{Co}(\text{NO}_3)_2 + \text{C}_6\text{H}_8\text{O}_7$  (or  $\text{CO}(\text{NH}_2)_2$ ) + DMF + calcination  $\rightarrow$  C or N doped  $\text{CoFe}_2\text{O}_4$ , and the schematic diagram of the simple experimental process is shown in Fig. 1. The citric acid and urea were the origin of doped C and N elements, and the concentrations were 0 mol·L<sup>-1</sup>, 0.05 mol·L<sup>-1</sup>, 0.1 mol·L<sup>-1</sup>, 0.18 mol·L<sup>-1</sup>, 0.3 mol·L<sup>-1</sup>, and 0.5 mol·L<sup>-1</sup> respectively. The obtained mix solution was calcined at 700 °C for 2 hour in air, and the heating rate was 1 °C/min. The obtained products were the C or N doped  $\text{CoFe}_2\text{O}_4$  nanoparticles.

The structure of nanoparticle was measured by X-ray diffraction (XRD, PANalytical X'Pert) equipped with Cu-K $\alpha$  radiation ( $\lambda = 1.5406 \text{ \AA}$ ). The morphology of sample was observed by using transmission electron microscopy (TEM, Tecnai<sup>TM</sup> G<sup>2</sup> F30, FEI) and field emission scanning electron microscopy (SEM, Hitachi S-4800) equipped with an energy-dispersive spectrometer. The X-ray photoelectron spectroscopy (XPS, PHI-5702, Physical Electronics) was performed using a monochromatic Mg-K $\alpha$  irradiation and a charge neutralizer, and all binding energies were referred to the C1s peak at 284.6 eV of the surface adventitious carbon. Mössbauer spectra were recorded at room temperature using a conventional constant acceleration spectrometer with a  $\gamma$ -ray source of 25 mCi <sup>57</sup>Co in a palladium matrix. The magnetic properties of the samples were measured using a vibrating sample magnetometer (VSM, Lakeshore 7304).

## Results and Discussion

The structures for all C-doped  $\text{CoFe}_2\text{O}_4$  samples with different citric acid concentration were performed by XRD, which is shown in Fig. 2. It can be seen that the samples show good single  $\text{CoFe}_2\text{O}_4$  phase with the cubic lattice

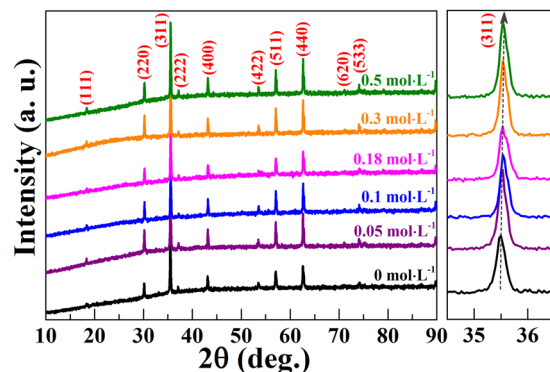


**Figure 2.** XRD patterns for all C-doped  $\text{CoFe}_2\text{O}_4$  samples with different citric acid concentrations.

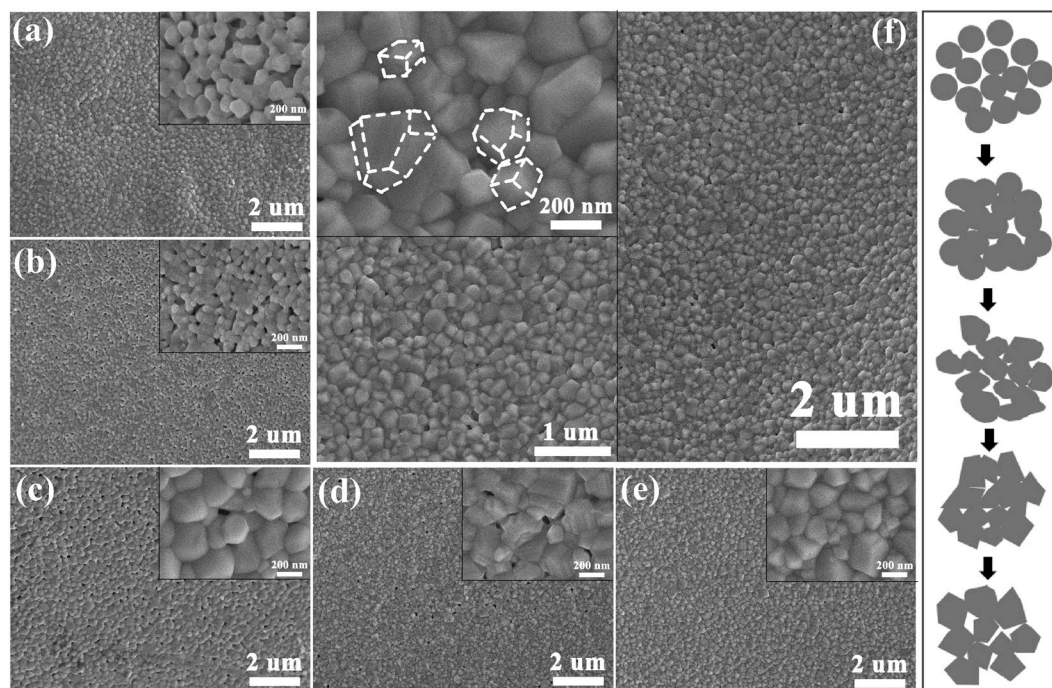


**Figure 3.** SEM images for all C-doped  $\text{CoFe}_2\text{O}_4$  samples with different citric acid concentration: (a)  $0 \text{ mol}\cdot\text{L}^{-1}$ , (b)  $0.05 \text{ mol}\cdot\text{L}^{-1}$ , (c)  $0.1 \text{ mol}\cdot\text{L}^{-1}$ , (d)  $0.18 \text{ mol}\cdot\text{L}^{-1}$ , (e)  $0.3 \text{ mol}\cdot\text{L}^{-1}$ , and (f)  $0.5 \text{ mol}\cdot\text{L}^{-1}$ , respectively. The inset in each picture is the amplifying results. The right picture is the simply formation process of the samples with the increase of citric acid concentration.

(JCPDS#22-1086) when the concentration of citric acid increases from  $0 \text{ mol}\cdot\text{L}^{-1}$  to  $0.5 \text{ mol}\cdot\text{L}^{-1}$ , and all the diffraction peaks are well indexed. The diffraction peaks (311) of the samples shift to the higher angles as citric acid concentration increases to  $0.18 \text{ mol}\cdot\text{L}^{-1}$ , and then almost keep unchanged. The results suggest a reduction of lattice with the improvement of citric acid concentration, which reveals the influence of additional citric acid on the structure of samples. Previous studies for the synthesis of zirconia showed the same variation with the improvement of citric acid content<sup>73,74</sup>. When urea is doped into  $\text{CoFe}_2\text{O}_4$  samples, the XRD patterns for N-doped  $\text{CoFe}_2\text{O}_4$  samples with different urea concentration are shown in Figure S1. It can be observed that the diffraction peaks (104) of  $\text{Fe}_2\text{O}_3$  are also observed except for the  $\text{CoFe}_2\text{O}_4$  phases when urea concentration increases from  $0 \text{ mol}\cdot\text{L}^{-1}$  to  $0.5 \text{ mol}\cdot\text{L}^{-1}$ . The main diffraction peaks (311) of  $\text{CoFe}_2\text{O}_4$  shifts to the higher angles as urea concentration increases to  $0.1 \text{ mol}\cdot\text{L}^{-1}$ , and then the peak keeps almost unchanged when the secondary phase  $\text{Fe}_2\text{O}_3$  exists in particles. The results indicate that the additional urea can affect the structure of  $\text{CoFe}_2\text{O}_4$  nanoparticles, but it will also introduce other impurities of  $\text{Fe}_2\text{O}_3$  when urea concentration is high. Previous works also showed that the excess of urea could cause additional hematite  $\text{Fe}_2\text{O}_3$  phase in ferrite nanoparticles<sup>75,76</sup>, and the gases generated by urea are easily released at the moment, which is adverse for the crystallization of ferrite<sup>75–78</sup>. Thus, the hematite  $\text{Fe}_2\text{O}_3$  phase is generated with the improvement of urea concentration.

Typical SEM images for all C-doped  $\text{CoFe}_2\text{O}_4$  samples with different citric acid concentration are shown in Fig. 3. Pure  $\text{CoFe}_2\text{O}_4$  nanoparticles showed in Fig. 3(a) are composed of a large quantity of uniform microspheres.

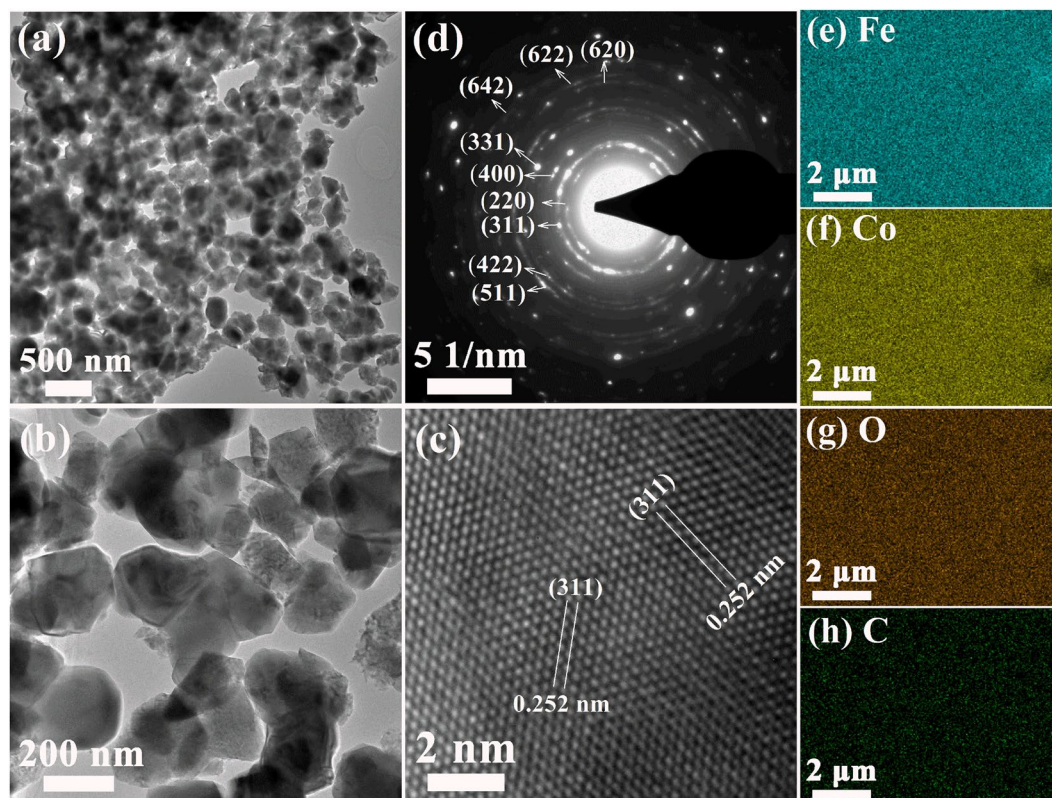


**Figure 4.** C-doped  $\text{CoFe}_2\text{O}_4$  sample with citric acid concentration of  $0.5 \text{ mol}\cdot\text{L}^{-1}$ . (a,b) Typical TEM images, (c) HRTEM image, (d) SAED; Elemental mappings: (e) Fe element; (f) Co element; (g) O element, and (h) C element.

The  $\text{CoFe}_2\text{O}_4$  particles begin to reunite together when citric acid is introduced to precursor (Fig. 3b), and the samples are composed of large and agglomerative particles which are surrounded by lots of small nanoparticles. As citric acid content is further increased (Fig. 3c), obvious smooth and compact nanoparticles can be seen, and the particle sizes increase. These results reveal that  $\text{CoFe}_2\text{O}_4$  nanoparticles are further grown when citric acid is added during the synthetic process, and the particles increase with the improvement of citric acid concentration. Afterwards,  $\text{CoFe}_2\text{O}_4$  particles begin to reunite together when citric acid concentration is  $0.18 \text{ mol}\cdot\text{L}^{-1}$  (Fig. 3d), and the samples change from near-spherical to irregular cubelike shapes. Then  $\text{CoFe}_2\text{O}_4$  nanoparticles become compact and irregular cubelike shapes with the further improvement of citric acid concentration, which are shown in Fig. 3(e,f). The average particles size is more than 200 nm when citric acid concentration is  $0.18 \text{ mol}\cdot\text{L}^{-1}$ . These formation process with the increase of citric acid concentration is simply described by the right picture of Fig. 3. In addition, it can be seen from SEM results that the particles size seems to increase with the improvement of citric acid concentration. The particle sizes obtained from SEM are not accurate due to the aggregation of the samples, and it is not shown here. One can deduce that the particles size increases and the shape changes to irregular cubelike shapes after the doping of C element. It is reported that the increasing citric acid contents can improve the degree of chelation of metallic ions in the solution, which results in a higher uniformity of metallic ions during the synthetic process<sup>79,80</sup>. It is also reported that the increasing concentration of citric acid can reduce the formation temperature of ferrite<sup>81</sup>, in other words, the ferrites are easier formed when the citric acid is added under the same calcination temperature. In this work, when citric acid is added in the precursors, the uniformity and dispersion of Fe and Co ions become better, the reactions of solution are more sufficient, and the local calcination temperature around ferrite molecule may be improved. These conditions could enhance the growth rate of particles, and the particle sizes increase. The growth rate of the particle increases faster with the further improvement of citric acid, and then results in the change of nanoparticle shape. It has been demonstrated that the shape of the nanoparticles can also be reversibly interchanged between spherical and cubic shape by controlling particles growth rate<sup>57</sup>. The SEM images for N-doped  $\text{CoFe}_2\text{O}_4$  samples with different urea concentration are similar to the results of C-doped  $\text{CoFe}_2\text{O}_4$  nanoparticles, which are shown in Figure S2.

As a representative, the morphology and structure for C-doped  $\text{CoFe}_2\text{O}_4$  with the citric acid concentration of  $0.5 \text{ mol}\cdot\text{L}^{-1}$  are further characterized by TEM. As shown in Fig. 4(a,b), the results indicate large and black areas of irregular cubelike  $\text{CoFe}_2\text{O}_4$  nanoparticles, and the average particles size is about 220 nm. HRTEM characterizations present the lattice fringes of the sample, and the interfringe distance shown in Fig. 4(c) is 0.252 nm, which is correspond well to {311} planar spaces of  $\text{CoFe}_2\text{O}_4$  nanoparticles. The SAED (Fig. 4d) clearly presents a group of atomic planes of the particles, revealing the highly crystalline nature of these nanoparticles. A large number of C-doped  $\text{CoFe}_2\text{O}_4$  nanoparticles with the citric acid concentration of  $0.5 \text{ mol}\cdot\text{L}^{-1}$  are used to investigate the

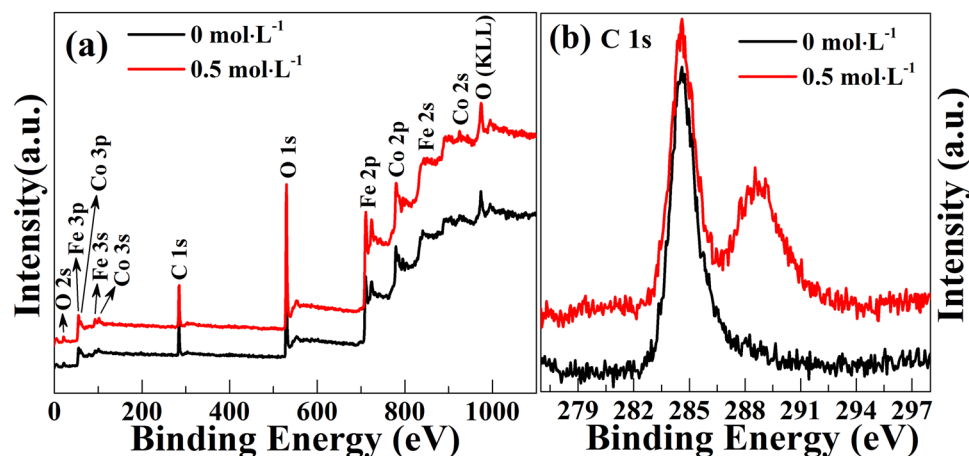


**Figure 5.** XPS data for the pure  $\text{CoFe}_2\text{O}_4$  ( $0 \text{ mol}\cdot\text{L}^{-1}$ ) and C-doped  $\text{CoFe}_2\text{O}_4$  samples with citric acid ( $0.5 \text{ mol}\cdot\text{L}^{-1}$ ): (a) the full scan, (b) C 1s level.

elemental distribution by using EDX mapping measurement. The impurities in the electron microscopy, e.g. carbon coated grids, has been avoided and excluded during the sample preparation to obtain an accurate results. As shown in Fig. 4(e–h), all Fe, Co, O and C elements distribute evenly and uniformly throughout the  $\text{CoFe}_2\text{O}_4$  nanoparticles, which confirm that C has been incorporated into the  $\text{CoFe}_2\text{O}_4$  nanoparticles. However, the mapping of C element does not display very obvious profile when compared to others, which can be concluded that a few C elements are incorporated into the nanoparticles. The EDX mapping measurement of N-doped  $\text{CoFe}_2\text{O}_4$  samples ( $0.18 \text{ mol}\cdot\text{L}^{-1}$ ) shown in Figure S2 also indicates that a few N contents are incorporated into  $\text{CoFe}_2\text{O}_4$  nanoparticles.

The elemental composition is examined by XPS to further distinguish the chemical composition of C-doped  $\text{CoFe}_2\text{O}_4$  nanoparticles, which is displayed in Fig. 5(a) shows the full scanned XPS spectra of the pure  $\text{CoFe}_2\text{O}_4$  ( $0 \text{ mol}\cdot\text{L}^{-1}$ ) and C-doped  $\text{CoFe}_2\text{O}_4$  ( $0.5 \text{ mol}\cdot\text{L}^{-1}$ ) samples. It can be seen that Co 2p, Fe 2p, O 1s and C 1s peaks appear in the pure  $\text{CoFe}_2\text{O}_4$  and C-doped  $\text{CoFe}_2\text{O}_4$ , and the full scan spectra of two samples show no obvious change. Figure 5(b) presents the C 1s core-level XPS spectra of two samples recorded in the high-resolution mode. It can be observed that one high peak is detected at about 284.6 eV, which belongs to the carbon contaminants adsorbed on the surface of the tested samples. However, C-doped sample also exhibits another obvious peak at about 288.8 eV, and this major contribution is assigned to C and O species<sup>82–85</sup>. As well known, the C atom is very small, which is difficult to substitute for the ions of  $\text{CoFe}_2\text{O}_4$ , and the XPS peak or spoor of C element in this work is not found at about 162 eV, indicating the absence of anionic carbon, i.e., there cannot exist the substitution between C and O elements<sup>86,87</sup>. The C element may be a interstitial one which is absorbed near the gap or edge of  $\text{CoFe}_2\text{O}_4$ <sup>88</sup>. The XPS data further prove that C element has been incorporated into  $\text{CoFe}_2\text{O}_4$  nanoparticles, which agrees well with XRD spectra and EDX mapping results.

The room temperature magnetic performances of products are discussed as below base on the understanding of the microstructure and chemical phase. As shown in Fig. 6(a), the magnetic hysteresis ( $M$ - $H$ ) loops reveal that all C-doped  $\text{CoFe}_2\text{O}_4$  samples perform a typical ferromagnetic property at room temperature. The magnetic saturation ( $M_s$ ) is about  $68 \text{ emu}\cdot\text{g}^{-1}$  for the pure  $\text{CoFe}_2\text{O}_4$ , which is close to the theoretical values of  $71.2 \text{ emu}\cdot\text{g}^{-1}$ <sup>89</sup>. The  $M_s$  of  $\text{CoFe}_2\text{O}_4$  nanoparticles monotonously increases with the improvement of citric acid concentration. The inset of Fig. 6(a) exhibits the citric acid concentration dependence of  $M_s$  of all samples. It can be seen when citric acid concentration reaches to  $0.5 \text{ mol}\cdot\text{L}^{-1}$ , the value of  $M_s$  increases to  $80 \text{ emu}\cdot\text{g}^{-1}$ , which is much larger than previously reported  $\text{CoFe}_2\text{O}_4$  nanoparticles<sup>39,40,54,55,65,69,71,89</sup>. Significantly, C-doped  $\text{CoFe}_2\text{O}_4$  nanoparticles in this work are quite different from the former metal-doped  $\text{CoFe}_2\text{O}_4$  nanoparticles, which mainly show a decreased  $M_s$  after doping, but the  $M_s$  is improved greatly in this work. Comparisons of the variability of  $M_s$  after doping are shown in Fig. 6(e). The results are consistent with our previous S-doped  $\text{CoFe}_2\text{O}_4$  nanoparticles<sup>5</sup>, which also showed an increasing  $M_s$  after the doping of S element. Both of the results reveal an approach to synthesize large scale ferrite nanoparticles, and improve the magnetic properties of ferrite nanoparticles.

Mössbauer spectroscopy gives information of the spatial orientation of a magnetic sublattice with respect to its net magnetization<sup>90</sup>, and the spectra for the pure  $\text{CoFe}_2\text{O}_4$  ( $0 \text{ mol}\cdot\text{L}^{-1}$ ) and C-doped  $\text{CoFe}_2\text{O}_4$  sample ( $0.5 \text{ mol}\cdot\text{L}^{-1}$ ) are shown in Fig. 6(b,c). The results show well-resolved two sextets due to  $\text{Fe}^{3+}$  at the tetrahedral (A) sites and another  $\text{Fe}^{3+}$  at octahedral (B) sites, and it presents a typical spinel structure reported by other authors<sup>56,62</sup>. The mössbauer parameters for two samples, i.e., hyperfine field ( $H_{\text{hf}}$ ) and isomer shift ( $\delta$ ) obtained from the mössbauer spectra are demonstrated in Fig. 6(d). The value of  $\delta$  at A site of C-doped  $\text{CoFe}_2\text{O}_4$  is decreased while it is increased at the B site, and this depends on the s-electron charged density of the absorber<sup>60</sup>. In addition, a little bigger  $H_{\text{hf}}$  of C-doped  $\text{CoFe}_2\text{O}_4$  is observed when comparing to pure  $\text{CoFe}_2\text{O}_4$ . These results indicate that  $\text{Co}^{2+}$  ions migrates from B site to A site and hence  $\text{Fe}^{3+}$  ions changes from A site to B site after doping of C element. As well known, the increasement of  $M_s$  can be achieved by either increasing of moments at site B and decreasing of moments at site A or both<sup>21</sup>. However, the changed site of A and B in this work is not the main reason for the improvement of  $M_s$ . The obtained values of mössbauer parameters for the samples are very close, and thier little

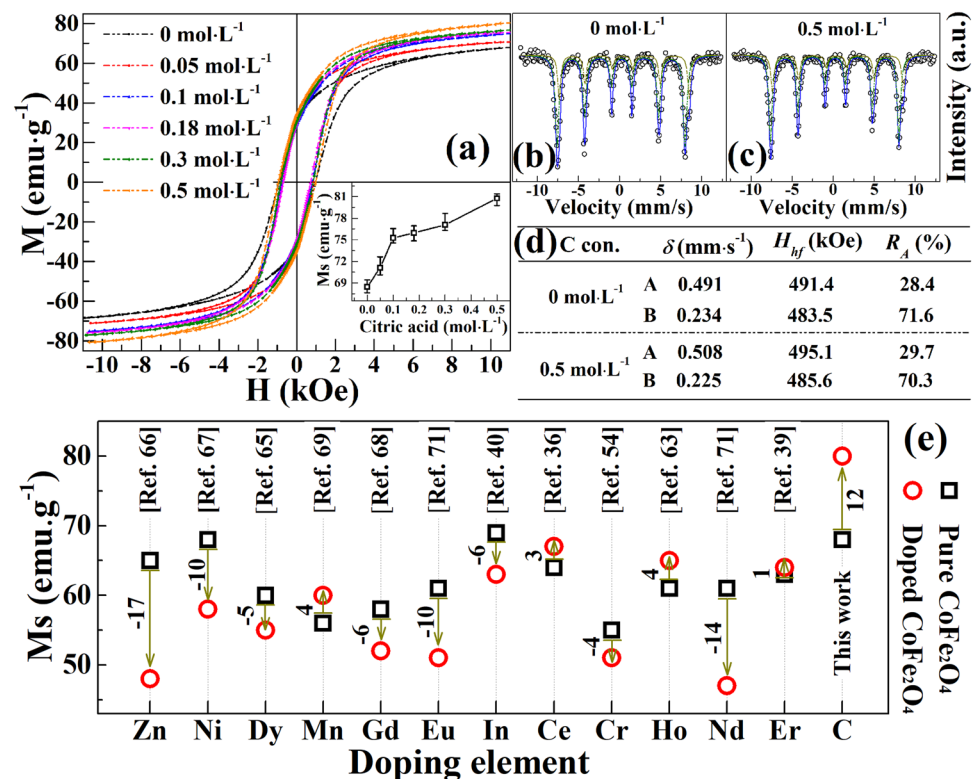


**Figure 6.** (a)  $M$ - $H$  loops for C-doped  $\text{CoFe}_2\text{O}_4$  nanoparticles with different citric acid concentration; the inset is citric acid concentration dependence of  $M_s$  for the corresponding samples. (b,c) Mössbauer spectra for the pure  $\text{CoFe}_2\text{O}_4$  (0 mol·L<sup>-1</sup>) and C-doped  $\text{CoFe}_2\text{O}_4$  nanoparticles (0.5 mol·L<sup>-1</sup>). (d) Mössbauer parameters for two samples obtained from the Mössbauer spectra. (e) Comparison of our work and other typical  $\text{CoFe}_2\text{O}_4$  nanoparticles for the variability of  $M_s$  after doping.

differences may mainly come from the calculated errors. Combining the results of previous S-doped  $\text{CoFe}_2\text{O}_4$ <sup>5</sup> and this work, the enhanced  $M_s$  of C-doped  $\text{CoFe}_2\text{O}_4$  nanoparticles is related to the improvement of the particle size and the change of particle shape as well as their higher crystallinity of the nanoparticles with the increased citric acid concentration. As shown in SEM and TEM results, the enhancement of citric acid amount causes the nanoparticles to synthesize the big particle size and high crystallinity, which results in the high magnetization of C-doped  $\text{CoFe}_2\text{O}_4$  nanoparticles. The enhanced  $M_s$  with the increase of nanoparticle size is similar to those results reported in other literature<sup>91</sup>, and it usually attributed to a decreasing proportion of the pinned surface magnetic moments in overall magnetization when the nanoparticle grows up in size<sup>92,93</sup>. In addition, previous research indicated the  $M_s$  of cubelike nanoparticles is larger than that of spherical nanoparticles<sup>57</sup>, and also demonstrated the higher crystallinity is benefited to enhanced the  $M_s$  of sample<sup>94,95</sup>. The flat surfaces of cubic nanoparticles enable the surface cations of metal to possess a more symmetric coordination, and the missing coordinating oxygen atoms is fewer when compared to the curved topologies of spherical nanoparticles. Therefore, the surface anisotropy should be much smaller in large cubelike nanoparticles, which would result in a smaller surface pinning and larger magnetization.

$M$ - $H$  loops for the N-doped  $\text{CoFe}_2\text{O}_4$  samples nanoparticles with different urea concentration are shown in Figure S3, the results reveal that the  $M_s$  of N-doped  $\text{CoFe}_2\text{O}_4$  nanoparticles has no obvious change, but decreases a little when compared to pure  $\text{CoFe}_2\text{O}_4$ . This is due to the presence of non-magnetic  $\text{Fe}_2\text{O}_3$  according to XRD results, which leads to the relative reduction of magnetic  $\text{CoFe}_2\text{O}_4$ , and the total qualities of magnetic moments drop. The urea concentration dependence of  $M_s$  of all samples is shown in the inset of Figure S3. Significantly, the  $M_s$  of  $\text{CoFe}_2\text{O}_4$  nanoparticles is not decreased sharply due to the non-magnetic  $\text{Fe}_2\text{O}_3$ , and there may exist two competitive relations in  $\text{CoFe}_2\text{O}_4$  nanoparticles. The first one, i.e. non-magnetic  $\text{Fe}_2\text{O}_3$ , plays a role to reduce the  $M_s$  of  $\text{CoFe}_2\text{O}_4$  nanoparticles, and the another one, i.e. the effect of doping element, promotes the improvement of the  $M_s$  of  $\text{CoFe}_2\text{O}_4$  nanoparticles. As a result, the  $M_s$  of N-doped  $\text{CoFe}_2\text{O}_4$  nanoparticles keeps a small fluctuation and does not increases or decreases sharply, which indirectly reflects that the  $M_s$  of  $\text{CoFe}_2\text{O}_4$  nanoparticles can be enhanced after doping with N element.

## Conclusion

Nonmetal-doped  $\text{CoFe}_2\text{O}_4$  nanoparticles were prepared via a facile calcination process in air. Characterizations of XRD, EDX mapping, XPS, and Mössbauer spectra results confirm that the C or N element is doped into  $\text{CoFe}_2\text{O}_4$  nanoparticles. The morphology of C or N doped  $\text{CoFe}_2\text{O}_4$  nanoparticles changes from the microsphere to the irregular cubelike nanoparticles due to the reduced formation temperature of ferrite by the additional

citric acid and urea, and their particles sizes also increase to more than 200 nm with the increasing citric acid or urea concentration. Particularly, the saturation magnetization of C-doped  $\text{CoFe}_2\text{O}_4$  nanoparticles increase to  $80 \text{ emu}\cdot\text{g}^{-1}$ , but the saturation magnetization of N-doped  $\text{CoFe}_2\text{O}_4$  has no obvious change due to the introduced non-magnetic  $\text{Fe}_2\text{O}_3$ . The results reveal an approach to synthesize large scale ferrite nanoparticles, and improve the magnetic properties of ferrite nanoparticles, and also provide the potential candidates to synthesize co-doped functional magnetic materials.

## References

- Maznichenko, I. V. *et al.* Impact of oxygen doping and oxidation state of iron on the electronic and magnetic properties of  $\text{BaFeO}_{3-\delta}$ . *Phys. Rev. B* **93**, 024411 (2016).
- Li, M. *et al.* Facile synthesis of electrospun  $\text{MFe}_2\text{O}_4$  (M=Co, Ni, Cu, Mn) spinel nanofibers with excellent electrocatalytic properties for oxygen evolution and hydrogen peroxide reduction. *Nanoscale* **7**, 8920–8930 (2015).
- Zhang, L. *et al.* Markedly enhanced coercive field and Congo red adsorption capability of cobalt ferrite induced by the doping of non-magnetic metal ions. *Chem. Eng. J.* **241**, 384–392 (2014).
- Gore, S. K. *et al.* Influence of  $\text{Bi}^{3+}$ -doping on the magnetic and Mossbauer properties of spinel cobalt ferrite. *Dalton Trans.* **44**, 6384–6390 (2015).
- Cao, D. *et al.* Nonmetal sulfur-doped coral-like cobalt ferrite nanoparticles with enhanced magnetic properties. *J. Mater. Chem. C* **4**, 951–957 (2016).
- Thi, T. M., Trang, N. T. H. & Van Anh, N. T. Effects of Mn, Cu doping concentration to the properties of magnetic nanoparticles and arsenic adsorption capacity in wastewater. *Appl. Surf. Sci.* **340**, 166–172 (2015).
- Imran, K. & Jisang, H. Manipulation of magnetic state in phosphorene layer by non-magnetic impurity doping. *New J. Phys.* **17**, 023056 (2015).
- Edström, A. *et al.* Magnetic properties of  $(\text{Fe}_{1-x}\text{Co}_x)_2$  mathrm B alloys and the effect of doping by 5d elements. *Phys. Rev. B* **92**, 174413 (2015).
- Giordano, F. *et al.* Enhanced electronic properties in mesoporous  $\text{TiO}_2$  via lithium doping for high-efficiency perovskite solar cells. *Nat. Commun.* **7** (2016).
- Lv, Q. *et al.* Ultrahigh capacitive performance of three-dimensional electrode nanomaterials based on  $\alpha\text{-MnO}_2$  nanocrystallines induced by doping Au through Å-scale channels. *Nano Energy* **21**, 39–50 (2016).
- Lee, B. H., Bazan, G. C. & Heeger, A. J. Doping-Induced Carrier Density Modulation in Polymer Field-Effect Transistors. *Adv. Mater.* **28**, 57–62 (2016).
- Ding, X., Ho, W., Shang, J. & Zhang, L. Self doping promoted photocatalytic removal of no under visible light with  $\text{bi2moo6}$ : Indispensable role of superoxide ions. *Appl. Catal. B: Environ.* **182**, 316–325 (2016).
- Li, W. *et al.* Magnetic Field-Controlled Lithium Polysulfide Semiliquid Battery with Ferrofluidic Properties. *Nano Letters* (2015).
- Xiong, P., Huang, H. & Wang, X. Design and synthesis of ternary cobalt ferrite/graphene/polyaniline hierarchical nanocomposites for high-performance supercapacitors. *J. Power Sources* **245**, 937–946 (2014).
- Shi, Y. *et al.* Ternary graphene– $\text{CoFe}_2\text{O}_4$ /CdS nanohybrids: preparation and application as recyclable photocatalysts. *J. Mater. Chem. A* **2**, 535 (2014).
- Xu, J., Li, Q., Zong, W., Zhang, Y. & Li, S. Ultra-wide detectable concentration range of GMR biosensors using  $\text{Fe}_3\text{O}_4$  microspheres. *J. Magn. Magn. Mater.* **417**, 25–29 (2016).
- Zhang, Y. *et al.* The influence of bias magnetization of nanoparticles on GMR sensor signal and sensitivity for the ultra-low concentration detection. *J. Magn. Magn. Mater.* **453**, 132–136 (2018).
- Bosca, M. *et al.* Effects of  $\text{Gd}^{3+}$ : Ag co-doping on structural and magnetic properties of lead tellurite glass ceramics. *Ceram. Int.* **42**, 1169–1176 (2016).
- Rasheed, S. *et al.* Effect of Li–Cu doping on structural, electrical and magnetic properties of cobalt ferrite nanoparticles. *Ceram. Int.* **42**, 3666–3672 (2016).
- Suresh, P., Babu, P. D. & Srinath, S. Role of (La, Gd) co-doping on the enhanced dielectric and magnetic properties of  $\text{BiFeO}_3$  ceramics. *Ceram. Int.* **42**, 4176–4184 (2016).
- Chakrabarty, S., Dutta, A. & Pal, M. Enhanced magnetic properties of doped cobalt ferrite nanoparticles by virtue of cation distribution. *J. Alloys Compd.* **625**, 216–223 (2015).
- Barbosa, D. A. B. *et al.* Ba-doping effects on structural, magnetic and vibrational properties of disordered  $\text{La}_2\text{NiMnO}_6$ . *J. Alloys Compd.* **663**, 899–905 (2016).
- Li, T.-Y. *et al.* Origins of the significant improvement in nanocrystalline Samarium–Cobalt's magnetic properties when doping with Niobium. *J. Alloys Compd.* **622**, 262–268 (2015).
- Park, M. H. *et al.* Ferroelectricity and Antiferroelectricity of Doped Thin  $\text{HfO}_2$ -Based Films. *Adv. Mater.* **27**, 1811–1831 (2015).
- Ham, Y. *et al.* Flux-mediated doping of  $\text{SrTiO}_3$  photocatalysts for efficient overall water splitting. *J. Mater. Chem. A* **4**, 3027–3033 (2016).
- Shim, J., Seo, Y.-S., Oh, B.-T. & Cho, M. Microbial inactivation kinetics and mechanisms of carbon-doped  $\text{TiO}_2$  (C- $\text{TiO}_2$ ) under visible light. *J. Hazard. Mater.* **306**, 133–139 (2016).
- Jiao, J. *et al.* Plasmonic silver nanoparticles matched with vertically aligned nitrogen-doped titanium dioxide nanotube arrays for enhanced photoelectrochemical activity. *J. Power Sources* **274**, 464–470 (2015).
- Duan, X., O'Donnell, K., Sun, H., Wang, Y. & Wang, S. Sulfur and Nitrogen Co-Doped Graphene for Metal-Free Catalytic Oxidation Reactions. *Small* **11**, 3036–3044 (2015).
- Ito, Y. *et al.* Tuning the Magnetic Properties of Carbon by Nitrogen Doping of Its Graphene Domains. *J. Am. Chem. Soc.* **137**, 7678–7685 (2015).
- Zhang, Y. *et al.* Nonmetal P-doped hematite photoanode with enhanced electron mobility and high water oxidation activity. *Energy Environ. Sci.* **8**, 1231–1236 (2015).
- Jiang, H. & Chen, C. Analysis and Calculation of Electronic Properties and Light Absorption of Defective Sulfur-Doped Silicon and Theoretical Photoelectric Conversion Efficiency. *J. Phys. Chem. A* **119**, 3753–3761 (2015).
- He, F. *et al.* The sulfur-bubble template-mediated synthesis of uniform porous g- $\text{C}_3\text{N}_4$  with superior photocatalytic performance. *Chem. Commun.* **51**, 425–427 (2015).
- Wang, C. *et al.* Sulfur-Doped Polyimide Photocatalyst with Enhanced Photocatalytic Activity under Visible Light Irradiation. *ACS Appl. Mat. Interface* **6**, 4321–4328 (2014).
- Yang, S. *et al.* Efficient synthesis of heteroatom (N or S)-doped graphene based on ultrathin graphene oxide-porous silica sheets for oxygen reduction reactions. *Adv. Funct. Mater.* **22**, 3634–3640 (2012).
- Kamala Bharathi, K., Balamurugan, K., Santhosh, P. N., Pattabiraman, M. & Markandeyulu, G. Magnetocapacitance in Dy-doped Ni ferrite. *Phys. Rev. B* **77**, 172401 (2008).
- Kahn, M. L. & Zhang, Z. J. Synthesis and magnetic properties of  $\text{CoFe}_2\text{O}_4$  spinel ferrite nanoparticles doped with lanthanide ions. *Appl. Phys. Lett.* **78**, 3651–3653 (2001).
- Sharma, R. K. *et al.* Variation of structural and hyperfine parameters in nanoparticles of Cr-substituted Co-Zn ferrites. *Phys. Rev. B* **75**, 144419 (2007).

38. Srivastava, R. C., Khan, D. C. & Das, A. R. Mossbauer and magnetic studies of Ti<sup>4+</sup>-substituted Ni-Zn ferrites. *Phys. Rev. B* **41**, 12514–12521 (1990).
39. Prathapani, S., Vinitha, M., Jayaraman, T. V. & Das, D. Effect of Er doping on the structural and magnetic properties of cobalt-ferrite. *J. Appl. Phys.* **115**, 17A502 (2014).
40. Nongjai, R., Khan, S., Asokan, K., Ahmed, H. & Khan, I. Magnetic and electrical properties of In doped cobalt ferrite nanoparticles. *J. Appl. Phys.* **112**, 084321 (2012).
41. Monaji, V. R. & Das, D. Influence of Zr doping on the structural, magnetic and magnetoelastic properties of cobalt-ferrites. *J. Alloys Compd.* **634**, 99–103 (2015).
42. Nlebedim, I. C., Hadimani, R. L., Prozorov, R. & Jiles, D. C. Structural, magnetic, and magnetoelastic properties of magnesium substituted cobalt ferrite. *J. Appl. Phys.* **113**, 17A928 (2013).
43. Liu, J., Bin, Y. & Matsuo, M. Magnetic Behavior of Zn-Doped Fe<sub>3</sub>O<sub>4</sub> Nanoparticles Estimated in Terms of Crystal Domain Size. *J. Phys. Chem. C* **116**, 134–143 (2012).
44. Xie, Y. *et al.* Effects of S and N doping on the structural, magnetic and electronic properties of rutile CrO<sub>2</sub>. *J. Magn. Magn. Mater.* **405**, 253–258 (2016).
45. Jia, H. *et al.* Effects of nonmetal (F, Si, B, and P) doping on the electronic structure and elastic properties of CeO<sub>2</sub>: A first-principles study. *J. Alloys Compd.* **666**, 419–424 (2016).
46. Hauksson, I. S., Simpson, J., Wang, S. Y., Prior, K. A. & Cavenett, B. C. Compensation processes in nitrogen doped ZnSe. *Appl. Phys. Lett.* **61**, 2208–2210 (1992).
47. Sinha, J., Banerjee, C., Chaurasiya, A. K., Hayashi, M. & Barman, A. Improved magnetic damping in CoFeB/MgO with an N-doped Ta underlayer investigated using the Brillouin light scattering technique. *RSC Adv.* **5**, 57815–57819 (2015).
48. Grebenyuk, G. S., Gomounova, M. V., Pronin, I. I., Senkovskiy, B. V. & Vyalikh, D. V. Effect of carbon doping on magnetic properties of Mn/Si interface. *J. Phys.: Conf. Ser.* **643**, 012096 (2015).
49. Giannopoulos, G. *et al.* Large magnetic anisotropy in strained Fe/Co multilayers on AuCu and the effect of carbon doping. *APL Mater.* **3**, 041103 (2015).
50. Drera, G. *et al.* Amorphous Si layers co-doped with B and Mn: Thin film growth and steering of magnetic properties. *Thin Solid Films* **590**, 148–155 (2015).
51. Ohno, T., Tsubota, T., Nakamura, Y. & Sayama, K. Preparation of S, C cation-codoped SrTiO<sub>3</sub> and its photocatalytic activity under visible light. *Appl. Catal. A: Gen.* **288**, 74–79 (2005).
52. Liu, K. W. *et al.* Electronic and magnetic properties of FeSe thin film prepared on GaAs (001) substrate by metal-organic chemical vapor deposition. *Appl. Phys. Lett.* **90**, 262503 (2007).
53. Li, X., Sun, X., Wang, J. & Liu, Q. Microstructure and magnetic properties of iron nitride thin films. *J. Alloys Compd.* **582**, 398–402 (2014).
54. Patange, S. M., Shirsath, S. E., Toksha, B. G., Jadhav, S. S. & Jadhav, K. M. Electrical and magnetic properties of Cr<sup>3+</sup> substituted nanocrystalline nickel ferrite. *J. Appl. Phys.* **106**, 023914 (2009).
55. Naik, S. R. & Salker, A. V. Change in the magnetostructural properties of rare earth doped cobalt ferrites relative to the magnetic anisotropy. *J. Mater. Chem.* **22**, 2740–2750 (2012).
56. Burianova, S., Vejpravova, J. P., Holec, P., Plocek, J. & Niznansky, D. Surface spin effects in La-doped CoFe<sub>2</sub>O<sub>4</sub> nanoparticles prepared by microemulsion route. *J. Appl. Phys.* **110** (2011).
57. Song, Q. & Zhang, Z. J. Shape Control and Associated Magnetic Properties of Spinel Cobalt Ferrite Nanocrystals. *J. Am. Chem. Soc.* **126**, 6164–6168 (2004).
58. Tirosh, E., Shemer, G. & Markovich, G. Optimizing cobalt ferrite nanocrystal synthesis using a magneto-optical probe. *Chem. Mater.* **18**, 465–470 (2006).
59. Ngo, A. T. & Pileni, M. P. Nanoparticles of Cobalt Ferrite: Influence of the Applied Field on the Organization of the Nanocrystals on a Substrate and on Their Magnetic Properties. *Adv. Mater.* **12**, 276–279 (2000).
60. Kumar, H. *et al.* Structural and magnetic study of dysprosium substituted cobalt ferrite nanoparticles. *J. Magn. Magn. Mater.* **401**, 16–21 (2016).
61. Wu, X., Yu, H., Dong, H. & Geng, L. Enhanced infrared radiation properties of CoFe<sub>2</sub>O<sub>4</sub> by single Ce<sup>3+</sup>-doping with energy-efficient preparation. *Ceram. Int.* **40**, 5905–5911 (2014).
62. Mohamed, M. B. & Yehia, M. Cation distribution and magnetic properties of nanocrystalline gallium substituted cobalt ferrite. *J. Alloys Compd.* **615**, 181–187 (2014).
63. Lohar, K. S., Pachpinde, A. M., Langade, M. M., Kadam, R. H. & Shirsath, S. E. Self-propagating high temperature synthesis, structural morphology and magnetic interactions in rare earth Ho<sup>3+</sup> doped CoFe<sub>2</sub>O<sub>4</sub> nanoparticles. *J. Alloys Compd.* **604**, 204–210 (2014).
64. Khandekar, M. S., Tarwal, N. L., Mulla, I. S. & Suryavanshi, S. S. Nanocrystalline Ce doped CoFe<sub>2</sub>O<sub>4</sub> as an acetone gas sensor. *Ceram. Int.* **40**, 447–452 (2014).
65. Karimi, Z. *et al.* Magnetic and structural properties of nano sized Dy-doped cobalt ferrite synthesized by co-precipitation. *J. Magn. Magn. Mater.* **361**, 150–156 (2014).
66. Hema, E., Manikandan, A., Karthika, P., Antony, S. A. & Venkatraman, B. R. A Novel Synthesis of Zn<sup>2+</sup>-Doped CoFe<sub>2</sub>O<sub>4</sub> Spinel Nanoparticles: Structural, Morphological, Opto-magnetic and Catalytic Properties. *J. Supercond. Nov. Magn.* **28**, 2539–2552 (2015).
67. Maaz, K. *et al.* Magnetic characterization of Co<sub>1-x</sub>Ni<sub>x</sub>Fe<sub>2</sub>O<sub>4</sub> (0 < x < 1) nanoparticles prepared by co-precipitation route. *Physica E* **41**, 593–599 (2009).
68. Peng, J. *et al.* Hydrothermal synthesis and magnetic properties of gadolinium-doped CoFe<sub>2</sub>O<sub>4</sub> nanoparticles. *J. Magn. Magn. Mater.* **323**, 133–137 (2011).
69. Cojocariu, A. M., Soroceanu, M., Hrib, L., Nica, V. & Caltun, O. F. Microstructure and magnetic properties of substituted (Cr, Mn) - cobalt ferrite nanoparticles. *Mater. Chem. Phys.* **135**, 728–732 (2012).
70. Dwivedi, G. D. *et al.* Existence of the multiferroic property at room temperature in Ti doped CoFe<sub>2</sub>O<sub>4</sub>. *Solid State Commun.* **152**, 360–363 (2012).
71. Amiri, S. & Shokrollahi, H. Magnetic and structural properties of RE doped Co-ferrite (RE=Nd, Eu, and Gd) nano-particles synthesized by co-precipitation. *J. Magn. Magn. Mater.* **345**, 18–23 (2013).
72. Zhao, L. *et al.* Magnetic properties of CoFe<sub>2</sub>O<sub>4</sub> ferrite doped with rare earth ion. *Mater. Lett.* **60**, 1–6 (2006).
73. Singh, K. A., Pathak, L. C. & Roy, S. K. Effect of citric acid on the synthesis of nano-crystalline yttria stabilized zirconia powders by nitrate–citrate process. *Ceram. Int.* **33**, 1463–1468 (2007).
74. Yang, J. *et al.* Synthesis of YSZ nanocrystalline particles via the nitrate–citrate combustion route using diester phosphate (PE) as dispersant. *Materials Letters* **57**, 2792–2797 (2003).
75. Costa, A. C. F. M., Morelli, M. R. & Kiminami, R. H. G. A. Combustion Synthesis: Effect of Urea on the Reaction and Characteristics of Ni-Zn Ferrite Powders. *J. Mater. Synth. Process.* **9**, 347–352 (2001).
76. Costa, A. C. F. M. *et al.* Effect of urea and glycine fuels on the combustion reaction synthesis of Mn-Zn ferrites: Evaluation of morphology and magnetic properties. *J. Alloys Compd.* **495**, 503–505 (2010).
77. Kasapoğlu, N., Baykal, A., Köseoğlu, Y. & Toprak, M. S. Microwave-assisted combustion synthesis of CoFe<sub>2</sub>O<sub>4</sub> with urea, and its magnetic characterization. *Scripta Materialia* **57**, 441–444 (2007).



78. Carp, O., Patron, L. & Reller, A. Coordination compounds containing urea as precursors for oxides—A new route of obtaining nanosized  $\text{CoFe}_2\text{O}_4$ . *Mater. Chem. Phys.* **101**, 142–147 (2007).
79. Yu, H.-F. & Huang, K.-C. Effects of pH and citric acid contents on characteristics of ester-derived  $\text{BaFe}_{12}\text{O}_{19}$  powder. *J. Magn. Magn. Mater.* **260**, 455–461 (2003).
80. Lee, K. K., Kang, Y. C., Jung, K. Y. & Kim, J. H. Preparation of nano-sized  $\text{BaTiO}_3$  particle by citric acid-assisted spray pyrolysis. *J. Alloys Compd.* **395**, 280–285 (2005).
81. Lee, W.-J. & Fang, T.-T. The effect of the molar ratio of cations and citric acid on the synthesis of barium ferrite using a citrate process. *J. Mater. Sci.* **30**, 4349–4354 (1995).
82. Stankovich, S. *et al.* Synthesis of graphene-based nanosheets via chemical reduction of exfoliated graphite oxide. *Carbon* **45**, 1558–1565 (2007).
83. Pei, S., Zhao, J., Du, J., Ren, W. & Cheng, H.-M. Direct reduction of graphene oxide films into highly conductive and flexible graphene films by hydrohalic acids. *Carbon* **48**, 4466–4474 (2010).
84. Liu, S., Tian, J., Wang, L. & Sun, X. A method for the production of reduced graphene oxide using benzylamine as a reducing and stabilizing agent and its subsequent decoration with Ag nanoparticles for enzymeless hydrogen peroxide detection. *Carbon* **49**, 3158–3164 (2011).
85. Hilder, M., Winther-Jensen, B., Li, D., Forsyth, M. & MacFarlane, D. R. Direct electro-deposition of graphene from aqueous suspensions. *Phys. Chem. Chem. Phys.* **13**, 9187–9193 (2011).
86. Goretzki, H., Rosenstiel, P. V. & Mandziej, S. Small area MXPS- and TEM-measurements on temper-embrittled 12% Cr steel. *J. Anal. Chem.* **333**, 451–452 (1989).
87. Kuivila, C., Butt, J. & Stair, P. Characterization of surface species on iron synthesis catalysts by X-ray photoelectron spectroscopy. *Appl. Surf. Sci.* **32**, 99–121 (1988).
88. Tang, X. & Li, D. Sulfur-Doped Highly Ordered  $\text{TiO}_2$  Nanotubular Arrays with Visible Light Response. *J. Phys. Chem. C* **112**, 5405–5409 (2008).
89. Bao, N., Shen, L., Wang, Y., Padhan, P. & Gupta, A. A Facile Thermolysis Route to Monodisperse Ferrite Nanocrystals. *J. Am. Chem. Soc.* **129**, 12374–12375 (2007).
90. Singh, J. P. *et al.* Magnetic study of nanostructured zinc ferrite irradiated with 100 MeV O-beam. *J. Magn. Magn. Mater.* **322**, 1701–1705 (2010).
91. Guo, P. *et al.* Facile Synthesis of  $\text{ZnFe}_2\text{O}_4$  Nanoparticles with Tunable Magnetic and Sensing Properties. *Langmuir* **29**, 8997–9003 (2013).
92. Chen, J. P. *et al.* Size-dependent magnetic properties of  $\text{MnFe}_2\text{O}_4$  fine particles synthesized by coprecipitation. *Phys. Rev. B* **54**, 9288–9296 (1996).
93. Šepelák, V. *et al.* Nanocrystalline Nickel Ferrite,  $\text{NiFe}_2\text{O}_4$ : Mechanosynthesis, Nonequilibrium Cation Distribution, Canted Spin Arrangement, and Magnetic Behavior. *J. Phys. Chem. C* **111**, 5026–5033 (2007).
94. Das, R. *et al.* Tunable High Aspect Ratio Iron Oxide Nanorods for Enhanced Hyperthermia. *J. Phys. Chem. C* **120**, 10086–10093 (2016).
95. Derang, C. *et al.* High saturation magnetization of  $\gamma\text{-Fe}_2\text{O}_3$  nano-particles by a facile one-step synthesis approach. *Sci. Rep.* **6**, 32360 (2016).

## Acknowledgements

This work is supported by National Natural Science Foundation of China (11704211, 11574121, 51371092, 11504192, 11604172, and 11674187), the basic scientific research business expenses of the central university, and Open Project of Key Laboratory for Magnetism and Magnetic Materials of the Ministry of Education, Lanzhou University.

## Author Contributions

Derang Cao synthesized the sample. Derang Cao, Jianbo Wang, and Qingfang Liu conceived the idea and wrote the manuscript based on input from all the authors. Lining Pan, Jianan Li, Xiaohong Cheng, and Zhong Zhao did the basic characterizations. Jie Xu, Qiang Li, Xia Wang, and Shandong Li discussed and give the suggestion to the paper.

## Additional Information

**Supplementary information** accompanies this paper at <https://doi.org/10.1038/s41598-018-26341-4>.

**Competing Interests:** The authors declare no competing interests.

**Publisher's note:** Springer Nature remains neutral with regard to jurisdictional claims in published maps and institutional affiliations.



**Open Access** This article is licensed under a Creative Commons Attribution 4.0 International License, which permits use, sharing, adaptation, distribution and reproduction in any medium or format, as long as you give appropriate credit to the original author(s) and the source, provide a link to the Creative Commons license, and indicate if changes were made. The images or other third party material in this article are included in the article's Creative Commons license, unless indicated otherwise in a credit line to the material. If material is not included in the article's Creative Commons license and your intended use is not permitted by statutory regulation or exceeds the permitted use, you will need to obtain permission directly from the copyright holder. To view a copy of this license, visit <http://creativecommons.org/licenses/by/4.0/>.

© The Author(s) 2018